

See discussions, stats, and author profiles for this publication at: <https://www.researchgate.net/publication/282890407>

Elucidating Hydrogen Oxidation/Evolution Kinetics in Alkaline and Acid Solutions via Optimizing Pt-Shell Thickness on Ru Core

ARTICLE in ACS CATALYSIS · OCTOBER 2015

Impact Factor: 9.31 · DOI: 10.1021/acscatal.5b01670

READS

29

10 AUTHORS, INCLUDING:



Yu Zhang

Brookhaven National Laboratory

11 PUBLICATIONS 212 CITATIONS

SEE PROFILE



Wei An

Shanghai University of Engineering Science

47 PUBLICATIONS 1,097 CITATIONS

SEE PROFILE



Ping Liu

Brookhaven National Laboratory

120 PUBLICATIONS 4,210 CITATIONS

SEE PROFILE



Jia Wang

Brookhaven National Laboratory

106 PUBLICATIONS 4,837 CITATIONS

SEE PROFILE

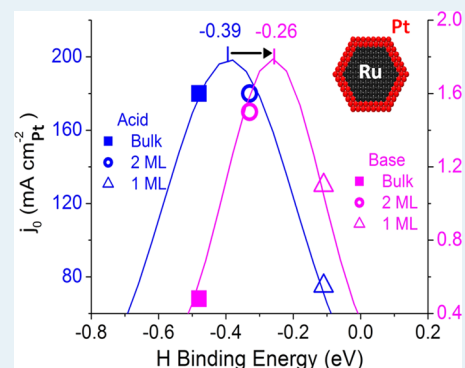
Elucidating Hydrogen Oxidation/Evolution Kinetics in Base and Acid by Enhanced Activities at the Optimized Pt Shell Thickness on the Ru Core

Katherine Elbert,[†] Jue Hu,[‡] Zhong Ma, Yu Zhang, Guangyu Chen,[§] Wei An,^{||} Ping Liu, Hugh S. Isaacs, Radoslav R. Adzic, and Jia X. Wang*

Chemistry Department, Brookhaven National Laboratory, Upton, New York 11973, United States

ABSTRACT: Hydrogen oxidation and evolution on Pt in acid are facile processes, while in alkaline electrolytes, they are 2 orders of magnitude slower. Thus, developing catalysts that are more active than Pt for these two reactions is important for advancing the performance of anion exchange membrane fuel cells and water electrolyzers. Herein, we detail a 4-fold enhancement of Pt mass activity that we achieved using single-crystalline Ru@Pt core-shell nanoparticles with two-monolayer-thick Pt shells, which doubles the activity on Pt–Ru alloy nanocatalysts. For Pt specific activity, the two- and one-monolayer-thick Pt shells exhibited enhancement factors of 3.1 and 2.3, respectively, compared to the Pt nanocatalysts in base, differing considerably from the values of 1 and 0.4, respectively, in acid. To explain such behavior and the orders of magnitude difference in activity on going from acid to base, we performed kinetic analyses of polarization curves over a wide range of potential from –250 to 250 mV using the dual-pathway kinetic equation. From acid to base, the activation free energies increase the most for the Volmer reaction, resulting in a switch of the rate-determining step from the Tafel to the Volmer reaction, and a shift to a weaker optimal hydrogen binding energy. The much higher activation barrier for the Volmer reaction in base than in acid is ascribed to one or both of the two catalyst-insensitive factors: slower transport of OH[–] than H⁺ in water and a stronger O–H bond in water molecules (HO–H) than in hydrated protons (H₂O–H⁺).

KEYWORDS: HOR, HER, alkaline fuel cells, water electrolysis, Ru@Pt core-shell



1. INTRODUCTION

The scarcity and high cost of platinum group metals (PGMs) remain an obstacle in widening the use of proton exchange membrane (PEM) fuel cells and water electrolyzers for reducing carbon emissions.^{1,2} A possible alternative is employing an anion exchange membrane (AEM)^{3,4} that offers a less corrosive environment, so allowing the incorporation of non-PGM catalysts for oxygen reduction and evolution. Recent advances demonstrated activities comparable to that of platinum (Pt) for oxygen reduction in AEM fuel cells^{5–9} and to that of iridium oxide for oxygen evolution in AEM water electrolyzers.^{10–14} However, for the hydrogen oxidation reaction (HOR) and the hydrogen evolution reaction (HER), Pt's activity remains superior to that of the non-PGM catalysts,³ even though it is lower by 2 orders of magnitude than that in an acid environment.^{15–17} Thus, developing catalysts that are better than Pt for the HOR and HER in base is important for improving the efficiency of the AEM devices and lowering PGM loadings.

Recent encouraging experimental results include a Pt-coated copper nanowire catalyst that, based on measurements on the rotating disk electrode (RDE) in 0.1 M KOH, exceeded the area- and mass-normalized exchange currents of Pt nanoparticles by 3.5 and 1.9 times, respectively.¹⁸ A boost of peak

power density in an AEM hydrogen fuel cell from 0.6 to 1.0 W cm^{–2} was achieved using Ru_{0.56}Pt_{0.43} alloy nanoparticles with a total metal loading of 0.4 mg cm^{–2} (0.24 and 0.16 mg cm^{–2} Pt and Ru, respectively) compared to 0.4 mg cm^{–2} Pt nanoparticles.¹⁹ For these catalysts, the authors ascribed the enhanced HOR activities mainly to the weakened hydrogen binding energy on Pt, but the existence of surface Cu and Ru might have played a minor role.

In this study, we synthesized single-crystalline Ru@Pt core-shell nanocatalysts with one- or two-monolayer (ML)-thick Pt shells using an economically viable method of synthesis,²⁰ and then we evaluated their HOR–HER performance on gas diffusion electrodes in 1 M KOH. Besides the practical significance of their activities being higher than those of the RuPt alloy catalysts, the atomically sharp core-shell interface and the uniformity of the Pt shell thickness verified in our previous work²⁰ made these well-defined core-shell nanocatalysts suitable for in-depth kinetic analyses for improving our understanding of the factors determining the HOR–HER activity.

Received: July 31, 2015

Revised: September 29, 2015

Published: October 5, 2015

Whether hydrogen binding energy (H-BE) is the sole descriptor for the HOR–HER activity remains debatable. Strmcnik et al.¹⁶ suggested that the HER–HOR activities on Ir and Pt_{0.1}Ru_{0.9} alloy are higher than that of Pt in alkaline solution and attributed the enhancement to the OH adsorption on the more oxophilic sites, viz., the defects on Ir, and surface Ru on the PtRu alloy. However, Durst et al.¹⁷ showed that the exchange current on carbon-supported catalysts declines in the order Pt > Ir > Pd both in acid (measured by the hydrogen pump method) and in base (measured by the rotating disk electrode method), suggesting that the H-BE is the sole descriptor for comparing the HER–HOR catalysts. In addition, these authors ascribed the lowered HER–HOR activities when going from acid to base to a strengthening of hydrogen binding, based on the positive shifts of the hydrogen adsorption/desorption peaks in the voltammetry curves. Later, Sheng et al.²¹ studied polycrystalline platinum in pH-buffered solutions, showing a consistent trend of lower HER–HOR activity with the more positive hydrogen adsorption/desorption peaks as pH increased. The authors correlated the peak potential to adsorption enthalpy using the equation $-FE_{\text{peak}} = \Delta H$ and referred to the deduced ΔH as pH-dependent H-BE. This is confusing. By definition, $\text{H-BE} = E(\text{metal-H}) - E(\text{metal}) - E(\text{H}_2)/2$ describes explicitly the binding strength between a metal surface and an adsorbed H atom in vacuum, which often is calculated using density functional theory (DFT). In contrast, the free energy of H adsorption is a thermodynamic property of the electrode–electrolyte interface, depending not only on the H–metal interaction but also on the interaction of H with solution species, and thus, it can vary with pH. Furthermore, rigorous methods of thermodynamic analysis have been developed using low-index Pt single crystals, which involve determining the free energy (ΔG) from the integrated charges of the voltammetry curves, the entropy (ΔS) from the temperature-dependent ΔG , and the enthalpy via $\Delta H = \Delta G + T\Delta S$; the Pt–H bond energies deduced from these measurements (called $E_{\text{Pt-H}}$ and equivalent to H-BE) are similar to those under vacuum conditions.^{22,23}

Our approach to gaining insights into the mechanistic issues included undertaking DFT calculations for the binding energies of H and OH and constructing reaction free energy diagrams based on the parameters obtained by fitting the polarization curves over a wide range of potential for well-defined Ru@Pt core–shell catalysts. In section 3, we first present the DFT results and then briefly describe the dual-pathway kinetic equation that uses as the four kinetic parameters the adsorption free energy for the reaction intermediate and the activation free energies for the three elementary reaction steps. We give the fits to the acid polarization curves to illustrate how we used these fitted parameters in constructing the free energy diagram for the HOR and HER.

In Results and Discussion, we first compare the Pt mass activities of carbon-supported one- and two-ML-thick Ru@Pt core–shell nanocatalysts with those of commercial RuPt/C and Pt/C nanocatalysts, based on the exchange currents determined in 1 M KOH using the hanging-strip gas diffusion electrode method.²⁴ Second, we present the results of fitting the area-specific polarization curves and, using the fitted free energies, elucidate (1) the dominant pathway and the correlation between the activation barrier for the rate-determining step and the apparent activation energy determined from temperature-dependent activities, (2) the effects of H-BE and electrolytes on the adsorption free energy for the HOR–

HER intermediate, and (3) the large increase in the activation barrier for the Volmer reaction going from acid to base, thereby resulting in a switch of the rate-determining step from the Tafel reaction to the Volmer reaction, and a shift to a weaker optimal H-BE.

2. EXPERIMENTAL SECTION

2.1. Synthesis of Carbon-Supported Ru@Pt Core–Shell Nanoparticles. In our typical synthesis of the carbon-supported Ru nanoparticles, we placed a 100 mL ethanol solution containing 300 μmol of RuCl_3 in a three-necked flask, which was refluxed at the boiling temperature maintained by an oil bath at 110 °C while the sample was vigorously stirred for 1 h; meanwhile, 100 mg of carbon powder (Ketjen black EC-600JD) was dispersed by sonication in 60 mL of ethanol for 45 min. The slurry was transferred into the reaction flask when the color of the RuCl_3 solution had changed from brown to green. We assured the complete transfer of carbon via rinsing with additional ethanol, so that the weight of the final product can be compared to the calculated values of the starting materials. After the temperature stabilized, 6 mL of a 0.2 M aqueous NaOH solution (900 μmol of OH^- equal to 3 times that of the 300 μmol of Ru precursor) was added dropwise while the sample was being stirred vigorously. If, after 2 h, the solution had not become colorless, viz., the signal that denotes the completion of Ru reduction, we added 150 μmol of NaOH (0.5 times the 300 μmol of Ru) and then refluxed the solution for an additional hour. After the solution had been cooled to room temperature, the carbon-supported Ru nanoparticles were filtered out, rinsed, and vacuum-dried. The as-synthesized Ru/C sample was annealed in H_2 at 450 °C for 1 h to enhance its crystallinity, thereby preventing its partial alloying with Pt during our next step of coating the Pt shells. The weight of carbon-supported Ru nanoparticles, Ru/C, was consistent with the value of 130.3 mg, calculated from 300 μmol of Ru and 100 mg of carbon.

To deposit the Pt shell, we again dispersed the Ru/C sample made with 300 μmol of Ru in 100 mL of ethanol and again refluxed it for 1 h at the boiling temperature maintained by an oil bath at 110 °C to remove any surface oxide on the Ru nanoparticles. After the solution had been cooled to room temperature, we added 6 mL of a 50 mM H_2PtCl_6 ethanolic solution (Pt:Ru atomic ratio of 1.0) while the mixture was being vigorously stirred to ensure their uniform dispersion. The mixture was held at an oil bath temperature of 80 °C for 2 h, and then we added NaOH dropwise in an amount equal to 0.5 times the Pt's molar amount ($0.5 \times 300 \mu\text{mol}$). After a further 0.5 h, the colorless mixture was cooled to room temperature and then filtered, washed, and vacuum-dried. This Ru₁@Pt₁ sample has metal weight percentages of 31% Pt and 16% Ru, with a balance of 53% carbon support.

2.2. Preparation of Gas Diffusion Electrodes (GDEs). Catalyst inks were prepared by dispersing the carbon-supported catalysts in a solution of deionized water, 2-propanol, ethanol, and Nafion (perfluorinated resin, equivalent weight of 1000, Aldrich). Typically, the dry mass of Nafion is equal to that of carbon; the volumes of water, 2-propanol, and ethanol are 40, 80, and 40 μL , respectively, for 1 mg of carbon for making the low-loading samples, and volumes of 30, 60, and 30 μL , respectively, for 1 mg of carbon were used for preparing high-loading samples. Water was added first and ethanol last because pouring alcohol on dry Pt-containing nanocatalysts may cause a spark and ignition. The mixture was sonicated in an ice bath for

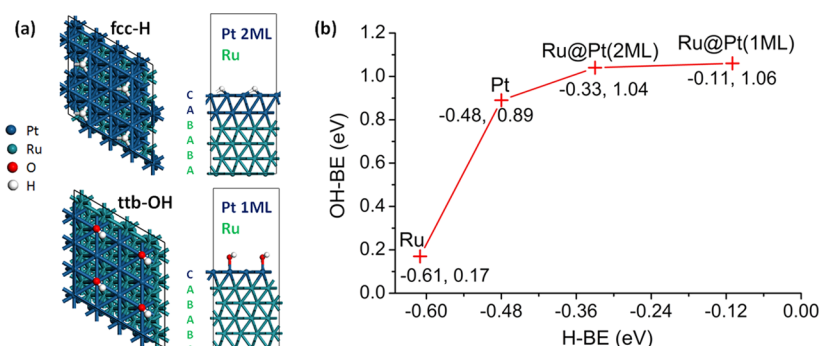


Figure 1. (a) Top and side views of optimized structures for 0.25-ML-coverage H and OH adsorbed on the close-packed (111) surface of a Pt bilayer and monolayer on hcp Ru. Adsorption sites: face-centered cubic (fcc) and top-to-bridge (ttb). (b) OH-BE vs H-BE on the close-packed surfaces of Ru(0001), Pt(111), the Pt bilayer, and the Pt monolayer.

10 min and mixed by shaking at a frequency of 12 s^{-1} for 1 h using a Mixer Mill MM 400 (Retsch). Before each usage, the ink was sonicated in an ice bath for 10 min. With an equal weight of Nafion as the carbon, the metal weight percentages in these catalyst inks, excluding solvents, were calculated by dividing the Pt (Ru) weight percent in the Ru@Pt/C catalyst by $(1 + \text{carbon weight } \%)$. For example, for a Ru₁@Pt₁/C catalyst with 31% Pt, 16% Ru, and 53% C, after it had been mixed with an equal weight of Nafion as the carbon, the metal weight percentages are 20.3% Pt and 10.5% Ru, balanced by an equal weight of carbon and Nafion.

Carbon papers, used as the gas diffusion layers (GDLs), were either Sigracet GDL 25 BC (from Ion Power) or Torey H90 paper (from the Fuel cell Store) coated with a layer of acid-treated carbon nanotubes. We weighed a GDL strip, 1.4 cm wide and 4 cm long, before brushing the catalyst ink over an area of 1 cm^2 ($1.4\text{ cm} \times 0.7\text{ cm}$) at one of its ends. After the solvents had evaporated completely, the increase in weight was used to calculate the metal loading from the weight percentage of metals in the Nafion-added catalyst mixture.

2.3. Electrochemical Measurements. All measurements were performed using a Voltalab PGZ 402 potentiostat. The reference electrodes for measuring in alkaline and acid solutions were a Hg/HgO,OH[−] electrode and a Ag/AgCl,Cl[−] electrode, respectively. We held a GDE strip vertically with its catalyst-coated end (1.4 cm wide, 0.7 cm high) completely immersed, but not too deeply, in a 1 M KOH or 1 M HClO₄ solution. It was positioned 1–2 cm away with the catalyzed side facing a Pt flag counter electrode. Such a hanging-strip GDE alleviates the limitation on gas transport by providing microporous channels within the GDE strip to allow gas directly into (during HOR) and out of (during HER) the nanocatalysts. We recorded cyclic voltammetry curves after purging the 1 M KOH electrolyte with argon. One hundred potential cycles between 0.05 and 0.95 V were run during preconditioning before measuring the HOR–HER performance. The electrolyte solution was saturated with hydrogen gas during the measurements of HER–HOR polarization, and the electrochemical impedance spectra. The steady-state polarization curves were obtained by averaging the currents measured during both the positive- and negative potential sweeps at a rate of 20 mV s^{-1} . An *iR* correction to the potential was made with the high-frequency resistance, determined by the electrochemical impedance spectra acquired at 0 V versus the reversible hydrogen electrode with a peak-to-peak perturbation of 10 mV at an ac frequency ranging from 20 kHz to 0.1 Hz. After HOR–HER measurements had been taken on the GDEs containing Pt-based

nanocatalysts, the H₂ in the electrochemical cells was purged with argon before removing the GDE strip from the solution; this was to avoid its ignition when hydrogen mixed with atmospheric oxygen.

2.4. Computational Method. The calculations were performed using periodic DFT as implemented in the Vienna ab initio simulation package (VASP).^{25,26} Ion–core electron interactions were described using the projected augmented wave method (PAW),^{27,28} and the Perdew–Wang functional (GGA-PW91) within the generalized gradient approximation (GGA)^{29,30} was used to describe the exchange–correlation effects. The cutoff energy of the plane wave basis set was 400 eV. To model the surfaces, $9 \times 9 \times 1$ k-points using the Monkhorst–Pack scheme³¹ and first-order Methfessel–Paxton smearing³² of 0.2 eV were employed in the integration to accelerate the convergence. The conjugate gradient algorithm was used in optimization, allowing the convergence of 10^{-4} eV in total energy, and 10^{-2} eV/Å in the Hellmann–Feynman force on each atom. All atoms were allowed to relax except those of the bottom two layers that were fixed at the hcp Ru bulk position with the following optimized lattice constants: $a = b = 2.731\text{ Å}$, and $c = 4.307\text{ Å}$.

3. THEORETICAL BACKGROUND

3.1. DFT Calculation of the Binding Energies of H and OH. We employed DFT to calculate the binding energies for H and OH as defined by $\text{H-BE} = E(\text{H/slab}) - [E(\text{slab}) + E(\text{H}_2/2)]$ and $\text{OH-BE} = E(\text{OH/slab}) - [E(\text{slab}) + E(\text{H}_2\text{O}) - E(\text{H}_2)/2]$, that is, the value of the difference in total energy between the H- or OH-adsorbed slab, and the sum of a bare metal slab and hydrogen, or in the addition of water (for OH-BE) molecules in the gas phase. The ordered core–shell Ru@Pt nanoparticles were modeled by a six-layer $p(2 \times 2)$ slab with a vacuum of 12 Å between the slabs as shown in Figure 1a, where two-ML Pt and one-ML Pt were supported on Ru(0001) with an energetically favorable stacking sequence.²⁰

Figure 1b plots the results, showing that both H binding and OH binding are weakened in the following order: Ru > Pt > Ru@Pt(2 ML) > Ru@Pt(1 ML). However, the changes are not proportional to each other. The trend is that a reactive Ru substrate/core (i.e., strong binding with adsorbates) causes the Pt surfaces and/or shells to be even less reactive than on a bulk Pt surface. This generally is the case for many adsorbates and is not sensitive to the details of adsorbates' coverage and adsorption sites.^{33,34} We previously calculated coverage-dependent H-BEs on Pt and attributed the positive adsorption

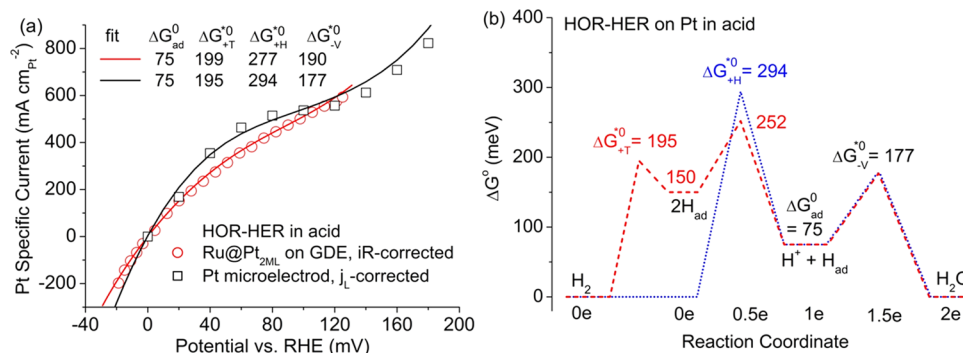
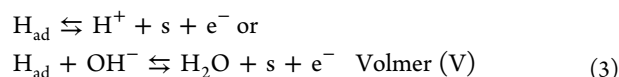
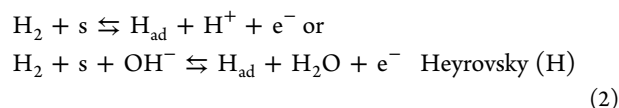
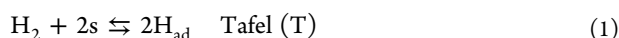


Figure 2. (a) Fits to the HOR–HER polarization curves for the Ru₁@Pt₁ bilayer catalyst (1.5 $\mu\text{g cm}^{-2}$ Pt) on a GDE and for a Pt microelectrode after correcting for mass transport.³⁷ (b) Free energy diagram for the HOR and HER at 0 V on Pt in acid, constructed using fitted parameters with the Tafel pathway (red line) and the Heyrovsky pathway (blue line).

free energy for the HOR–HER intermediate at 0 V to the considerable lateral repulsion among H adatoms, including both the HOR–HER intermediate at top sites and the underpotentially deposited H in hollow/bridge sites.³⁵ Here, we use the values of H–BE and OH–BE at a fixed coverage to show the trend among different catalysts.

3.2. Dual-Pathway Kinetic Equation and Free Energy Diagram for the HOR and HER. The Butler–Volmer equation, $j = j_0(e^{\eta/b} - e^{-\eta/b})$, is commonly used in evaluating the activities of the HOR and HER with its two parameters: the exchange current, j_0 , and the Tafel slope, b , or the transfer coefficient, α , that is included in b . However, it often cannot adequately describe the observed kinetic behavior over the entire potential range of interest because the Tafel slopes often vary with the overpotential, η . On the basis of the well-established kinetic model of two pathways with three elementary reaction steps, we derived a dual-pathway kinetic equation using four standard free energies as the adjustable parameters,^{35,36} wherein the transfer coefficients are fixed at 0.5 for the elementary steps (s stands for a surface site):



Because the adsorbed reaction intermediate is the same in acid and base, the formula of the dual-pathway equation is the same for the HOR–HER intermediate in both electrolytes, but the free energy parameters differ because they depend on both catalysts' properties and the electrolytes. In our previous derivation, we used the descriptive words “dissociative adsorption (DA)” for the Tafel reaction (T) and “oxidative adsorption (OA)” for the Heyrovsky (H) and “oxidative desorption (OD)” for the Volmer (V) reactions, from the viewpoint of the HOR.³⁵ With both the HOR and HER under consideration, it is appropriate to use the directionless notation of T–H–V with + and – signs, respectively, for the HOR and the HER. Thus, we have the total kinetic current, $j_k = j_T + j_H$ with

$$j_T = j_{+T} - j_{-T} = j^* e^{-\Delta G_{+T}^0/kT} [(1 - \theta)^2 - e^{2\Delta G_{ad}^0/kT} \theta^2] \quad (4)$$

$$\begin{aligned} j_H &= j_{+H} - j_{-H} \\ &= j^* e^{-\Delta G_{+H}^0/kT} [e^{0.5\eta/kT} (1 - \theta) - e^{\Delta G_{ad}^0/kT} e^{-0.5\eta/kT} \theta] \end{aligned} \quad (5)$$

The net currents of an elementary reactions are expressed by the differences, e.g., $j_{+H} - j_{-H}$; $j^* = 1000 \text{ A cm}^{-2}$ is a fixed reference prefactor, and $kT = 25.51 \text{ meV}$ at 23 °C. The four variable kinetic parameters are the standard (at zero overpotential) free energies of adsorption for the reaction intermediate, H_{ad} (ΔG_{ad}^0), and the standard activation free energies for the three elementary reaction steps (ΔG_{+T}^* , ΔG_{+H}^* , and ΔG_{-V}^*). The asterisk means the values for the activation free energies are tied to the prefactor of j^* while ΔG_{ad}^0 is not.³⁵ The adsorption isotherm, θ , is the fractional coverage for H_{ad} as a function of the overpotential, η , which was derived by solving the steady-state equation $d\theta/dt = 2\nu_T + \nu_H - \nu_V = 0$, where ν is the reaction rate. For θ to remain invariant with time, the reaction rates of the three elementary reactions must satisfy the equilibrium between the numbers of H atoms adsorbed via the Tafel reaction (two H_{ad} per H_2) and the Heyrovsky (one H_{ad} per H_2) reactions, $2\nu_T + \nu_H$, and that desorbed via the Volmer reaction, ν_V . The solution can be expressed as

$$\theta = \frac{-B - \sqrt{B^2 - 4AC}}{2A}, A \neq 0; \theta = -\frac{C}{B}, A = 0 \quad (6)$$

in which

$$\begin{aligned} A &= 2g_{+T} - 2g_{-T}, \\ B &= -4g_{+T} - g_{+H} - g_{-H} - g_{+V} - g_{-V}, \\ C &= 2g_{+T} + g_{+H} + g_{-V} \end{aligned}$$

The expressions for g_i are given below, with +i and –i for the reactions (T or H or V) in the HOR (+) and HER (–) direction:

$$\begin{aligned} g_{+T} &= \exp(-\Delta G_{+T}^0/kT), \\ g_{-T} &= \exp[-(\Delta G_{+T}^0 - 2\Delta G_{ad}^0)/kT] \\ g_{+H} &= \exp[-(\Delta G_{+H}^0 - 0.5\eta)/kT], \\ g_{-H} &= \exp[-(\Delta G_{+H}^0 - \Delta G_{ad}^0 + 0.5\eta)/kT] \\ g_{+V} &= \exp[-(\Delta G_{-V}^0 - \Delta G_{ad}^0 - 0.5\eta)/kT], \\ g_{-V} &= \exp[-(\Delta G_{-V}^0 + 0.5\eta)/kT] \end{aligned}$$

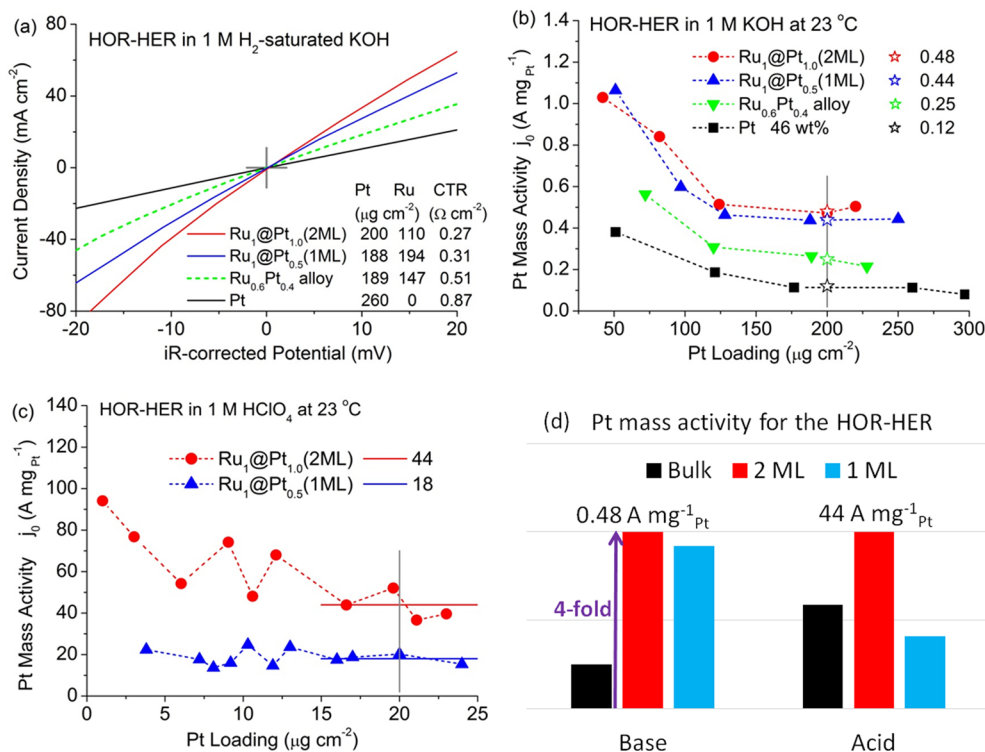


Figure 3. (a) Typical HOR–HER polarization curves for carbon-supported nanocatalysts on 1 cm² GDEs in 1 M KOH. (b and c) Pt mass-normalized exchange currents as a function of Pt loading for the HOR–HER in base and acid, respectively. (d) Comparison of the Pt mass activities of the Pt (black), Ru₁@Pt₁(2 ML) (red), and Ru₁@Pt_{0.5}(1 ML) (blue) nanocatalysts. The heights of the bars are normalized to the maximal value of 0.48 A (mg of Pt)^{−1} in base and that of 44 A (mg of Pt)^{−1} in acid.

Figure 2a shows the best fit (solid lines) to the polarization curves in acid. We used a very low Pt loading in measuring the Ru@Pt core–shell catalyst to reduce the current's magnitude and, thus, the effect of mass transport because of the exceptionally high reaction rate in acid. Our Ru@Pt curve is similar to the curve for the Pt that was based on the measurements using a Pt microelectrode reported by Chen and Kucernak.³⁷ The difference is not significant because it lies within the experimental uncertainties in determining the Pt's surface area with very low-loading nanocatalysts and with a single-particle Pt microelectrode.

We illustrate in Figure 2b a free energy diagram constructed using four fitted standard free energies, ΔG_{+T}^{*0} , ΔG_{ad}^0 , ΔG_{+H}^{*0} , and ΔG_{-V}^{*0} , for visualizing the reaction barriers for the HOR (+ direction) and HER (− direction) in two reaction pathways. In the construction of the Tafel pathway, the level at 150 meV for two adsorbed H atoms is determined by $2\Delta G_{ad}^0$ and that at 252 meV is obtained by $(\Delta G_{-V}^{*0} - \Delta G_{ad}^0) - 2\Delta G_{ad}^0$, so that the barriers for the first (252 − 150) and second (177 − 75) desorption of H_{ad} are the same. Within each pathway, the reaction rate largely is determined by the highest barrier, which is 195 meV for the HOR and 177 meV for the HER in the Tafel pathway (red line) and 294 meV for the HOR and 219 meV for the HER in the Heyrovsky pathway (blue line). As the activation barriers at 0 V are lower for the Tafel reaction than for the Heyrovsky reaction, the Tafel pathway dominates at small overpotentials.

4. RESULTS AND DISCUSSION

4.1. Pt Mass Activities for the HOR–HER on Pt and RuPt Nanocatalysts.

We synthesized Ru@Pt core–shell

nanoparticles on carbon supports using an economically viable method that produces single crystalline nanoparticles with a sharp, ordered core–shell interface.²⁰ By coating Pt on Ru cores with Pt:Ru atomic ratios of 0.5 and 1.0, we made carbon-supported nanocatalysts with dominant one- and two-ML Pt shells, which we designated as the Ru₁@Pt_{0.5}(1 ML) and Ru₁@Pt₁(2 ML) catalysts, respectively. Their HOR–HER activities were evaluated in comparison with those of commercial Pt/C (46 wt % Pt) and Ru_{0.6}Pt_{0.4}/C (30 wt % Pt and 23.3 wt % Ru) from Tanaka Kikinokoku International, Inc. The alloy particles are considered to have Pt and Ru atoms at the surface and in the inner core.

The HOR–HER activities in hydrogen-saturated 1 M KOH were measured using the hanging-strip GDE method.²⁴ The microporous layer in the GDE provides gas channels right to the catalysts, thereby allowing the HOR current to reach 600 mA without the gas diffusion limitation seen in the RDE measurements. Within ±20 mV, the HOR–HER polarization curves are nearly linear, as shown in Figure 3a. We obtained the charge transfer resistance (CTR) at 0 V from the linear fits within ±8 mV. A smaller CTR signifies higher activity; thus, the performances are in the order Ru₁@Pt₁(2 ML) > Ru₁@Pt_{0.5}(1 ML) > Ru_{0.6}Pt_{0.4} alloy > Pt. For comparing the Pt mass-normalized activities, it is convenient to convert the CTR to the exchange current, *j*₀, as defined in the Butler–Volmer equation, $j = j_0[e^{\alpha\eta/kT} - e^{-(1-\alpha)\eta/kT}]$, where α is the transfer coefficient, η is the overpotential, k ($=8.617 \times 10^{-5}$ eV K^{−1}) is the Boltzmann constant, and T is the temperature. At a small overpotential, the linear approximation holds for an exponential function, which leads to $j = j_0\eta/kT$ and $dj/d\eta = j_0/kT = 1/CTR$. At 296 K, we have j_0 (mA cm^{−2}) = 25.51 (mV)/CTR (Ω cm²).

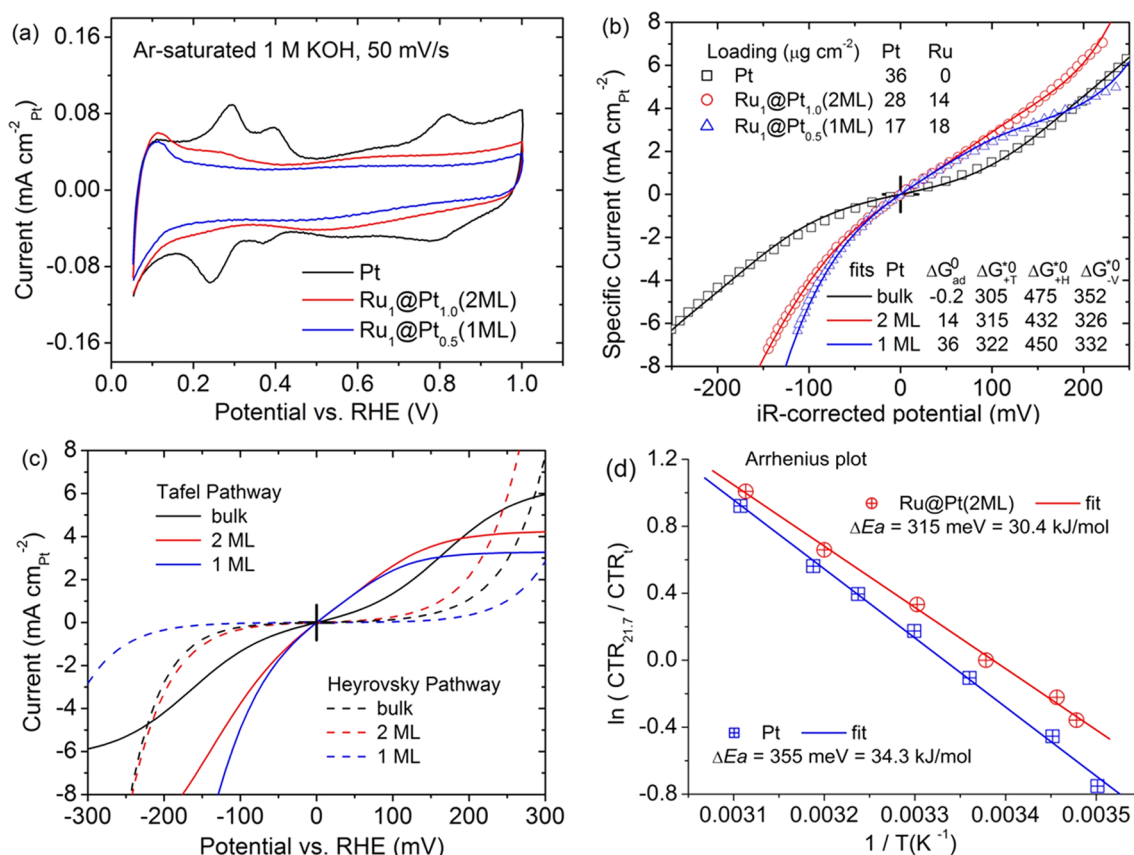


Figure 4. (a) Pt surface area-normalized voltammetry curves. (b) Pt-specific polarization curves for the HOR-HER (symbols) obtained on GDEs in hydrogen-saturated 1 M KOH at 23 °C with the best fits (—) using the dual-pathway kinetic equation. The values given for the fitted standard free energies are in units of millielectronvolts. (c) Currents via the Tafel (—) and Heyrovsky (---) reaction pathways. (d) Arrhenius plot for determining apparent activation energies for the HOR-HER on Pt (blue) and Ru₁@Pt_{1.0}(2 ML) (red) catalysts in 1 M KOH.

We obtained the exchange currents from measured CTRs for the four nanocatalysts on GDE samples made with a wide range of Pt loadings. The results are shown in Figure 3b by plotting the Pt mass-normalized exchange currents as a function of their Pt loadings. In the absence of any mass transport effects, the exchange current should be proportional to the catalyst's loading, and thus, the loading-normalized values should be a constant in the plot. The fact that all four catalysts have higher Pt mass activities at lower loadings indicates a likely ionic mass transport effect. A thinner layer of the catalyst reduces OH⁻ transport resistance, and the lower current also is affected less by transport. Because sufficient loading for high performance often is the top priority in practical applications, we used the values at 200 μg cm⁻² (marked by the crosses) for determining the enhancement factors in Pt mass activity, which is within the region of nearly constant activities. Compared to the Pt catalysts, the three Ru-containing catalysts exhibited enhancement factors in Pt mass activity of 4.0 for Ru₁@Pt_{1.0}(2 ML), 3.7 for Ru₁@Pt_{0.5}(1 ML), and 2.1 for the Ru_{0.6}Pt_{0.4} alloy.

The doubling of the Pt mass activity for the Ru_{0.6}Pt_{0.4} alloy versus Pt catalysts is equivalent to a 1.42-fold higher current with equal total metal loadings. This value is consistent with a boost of peak power density from 0.6 to 1.0 W cm⁻² (~1.67 times higher) in the AEM hydrogen fuel cell by using Ru_{0.56}Pt_{0.43} alloy nanoparticles with the same 0.4 mg cm⁻² total metal loading as with 0.4 mg cm⁻² Pt nanoparticles.¹⁹ Thus, the enhancement in Pt mass activity on the Ru₁@Pt_{1.0}(2 ML) is twice as high as that on the Ru_{0.6}Pt_{0.4} alloy, so

convincingly indicating the benefit of having all Pt atoms in the top surface layers.

On the basis of our previously measured CTRs in acid,²⁴ we show the Pt mass exchange currents for Ru₁@Pt_{1.0}(2 ML) and Ru₁@Pt_{0.5}(1 ML) in Figure 3c. The difference in scale from that in base is a factor of 100, and the ratio between the bilayer and monolayer is higher in acid than in base. The bar chart in Figure 3d is made by normalizing the mass exchange currents to the maximal values obtained with the Ru₁@Pt_{1.0}(2 ML) catalyst. The difference, by 2 orders of magnitude, between the values in acid and in base is consistent with the acid/base activity ratios of ~100-fold for Pt, Ir, and Pd, as determined using the hydrogen pump method for acids, and the RDE for alkaline electrolytes.¹⁷ To gain a better understanding of these phenomena, we next analyzed the polarization curves over a wide potential region with the currents normalized to the Pt surface area.

4.2. Kinetic Analyses of Pt Specific Activities for the HOR and HER. For studying the specific activity per Pt surface area, low-loading samples with a similar Pt surface area were used to minimize mass transport effects for use in analyses by fitting with the calculated kinetic currents. Panels a and b of Figure 4 show Pt surface area-normalized voltammetry and polarization curves for the Pt, Ru₁@Pt_{1.0}(2 ML), and Ru₁@Pt_{0.5}(1 ML) nanocatalysts. For the Pt sample, a Pt surface area of 23.4 cm² was determined from the integrated hydrogen desorption charge with 0.21 mC cm⁻², as is commonly used.²¹ The Pt surface areas for the bilayer and monolayer catalysts

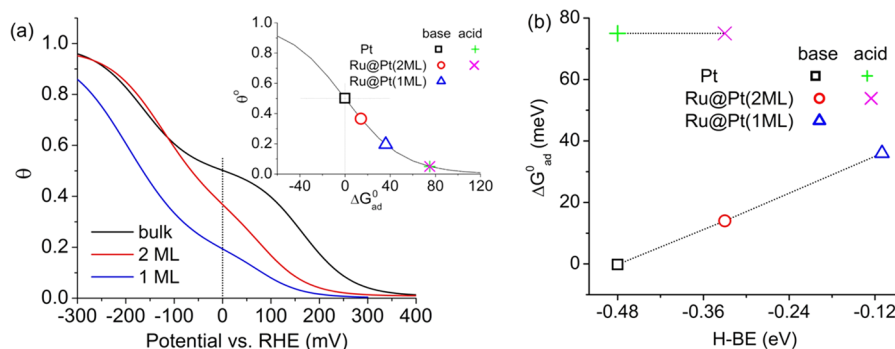


Figure 5. (a) Fractional coverage of the HOR–HER reaction intermediate, H_{ad} , as a function of potential. The inset shows the coverage of H_{ad} at 0 V vs the standard adsorption free energy. (b) ΔG_{ad}^0 obtained from fitting the HOR–HER polarization curves in base and acid vs the DFT-calculated H-BE.

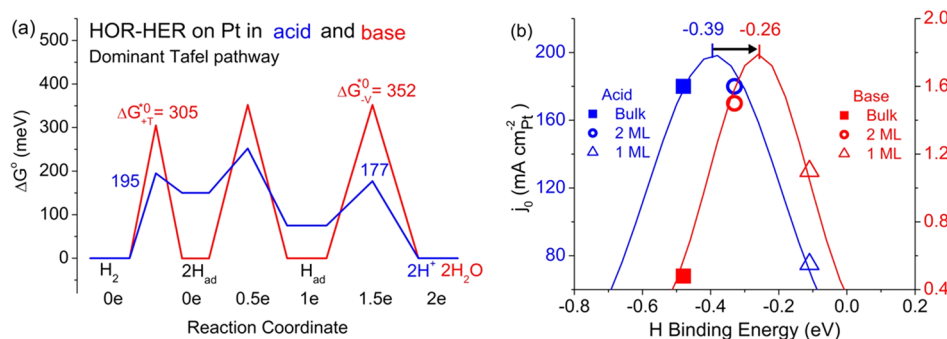


Figure 6. (a) Free energy diagram of the dominant Tafel pathway for the HOR (left to right) and the HER (right to left) on Pt in acid (blue) and base (red). (b) HOR–HOR specific activities for Pt(bulk), $Ru_1@Pt_1(2\text{ ML})$, and $Ru_1@Pt_{0.5}(1\text{ ML})$ in acid (blue) and in base (red) vs DFT-calculated H-BE.

were estimated using 1.0 and 1.7 cm² ($\mu\text{g of Pt}$)⁻¹, respectively, based on calculating the geometrical area from average particle sizes, and the CO-stripping measurement in previous studies.³⁸ The hydrogen adsorption at <0.4 V and the hydroxide adsorption at >0.5 V are both weakened in the following order: Pt > $Ru_1@Pt_1(2\text{ ML})$ > $Ru_1@Pt_{0.5}(1\text{ ML})$ (as shown in Figure 4a). These trends are consistent with those of calculated H-BEs and OH-BEs for bulk, bilayer, and monolayer Pt (section 3.1).

Figure 4b shows the Pt surface area-normalized polarization curves over a wide range of overpotentials. The shapes of the curves contain the information about the mechanism of the HOR–HER. We fitted the experimental data (symbols) using the dual-pathway kinetic equation given in section 3.2. The solid lines are the best fits and largely reproduced the measured curves. From the fitted free energy parameters given in Figure 4b, we found two common features for all three catalysts. First, the activation barrier is lower for the Tafel reaction than it is for the Heyrovsky reaction at 0 V, i.e., $\Delta G_{+H}^0 > \Delta G_{+T}^0$, meaning that the Tafel–Volmer (also the Volmer–Tafel) pathways dominate at low overpotentials. This fact is illustrated in Figure 4c by the calculated currents of the Tafel pathway (j_T , solid lines) and the Heyrovsky pathway (j_H , dashed lines). Comparing each pair of the currents reveals $j_T > j_H$ within ± 200 mV, and the contribution from the Heyrovsky pathway becomes significant with >100 mV overpotentials. Second, the activation barrier is higher for the Volmer reaction than the Tafel reaction, i.e., $\Delta G_{-V}^0 > \Delta G_{+T}^0$, so that the Volmer reaction is the rate-determining step in the dominant pathway for all three catalysts.

In a manner independent of the fitting polarization curves, we determined the apparent activation barrier, ΔE_a , from the temperature-dependent activity measured by the CTR at 0 V. The determined ΔE_a is for the overall reaction rate, which should be comparable with the standard activation free energy for the rate-determining step in the dominant pathway. As shown in Figure 4d, the value deduced from the Arrhenius plots is 355 meV, close to the ΔG_{-V}^0 of 352 meV for Pt. Also, the ΔE_a of 326 meV is close to the ΔG_{-V}^0 of 315 meV for $Ru_1@Pt_1(2\text{ ML})$. The uncertainty in ΔE_a often is $\sim 10\%$ as we showed in details of the temperature-dependent measurement for the $Ru_1@Pt_1(2\text{ ML})$ catalyst in acid, for which the apparent activation energy (ΔE_a) is 200 meV.²⁴ This value again is consistent with the ΔG_{+T}^0 of 195 meV, the activation free energy for the rate-determining step in the dominant pathway in acid (Figure 2b).

We next discuss the correlation between the standard free energies of adsorption obtained from fitting measured polarization curves, ΔG_{ad}^0 , and the DFT-calculated H-BE. Figure 5a shows the adsorption isotherm, $\theta(\eta)$, for the HOR–HER intermediate (H_{ad}) calculated with eq 6 using the fitted parameters given in Figure 4b. The value at 0 V, θ^0 , is derived solely from the ΔG_{ad}^0 definition $\theta^0/(1 - \theta^0) \equiv \exp(-\Delta G_{ad}^0/kT)$,³⁵ and thus, $\theta^0 = \exp(-\Delta G_{ad}^0/kT)/(1 + \exp(-\Delta G_{ad}^0/kT))$ as shown in the inset of Figure 5a. For the three catalysts in alkaline solutions, the fitted ΔG_{ad}^0 values are linearly correlated with the DFT-calculated H-BE (Figure 5b), indicating the major role of the H–Pt bonding strength in setting the trend in the H adsorption free energy. However, the electrolytes also strongly influenced the magnitude of the adsorption free energy. The decreases in ΔG_{ad}^0 on going from acid to base

suggest a strengthening of H adsorption, coinciding with the strengthened H adsorption deduced from the positive shift of the H adsorption/desorption peaks in the voltammetry curves with an increase in pH.²¹ For Pt in acids, we verified an adsorption isotherm for the HOR–HER intermediate using *in situ* infrared spectroscopy to monitor atop-site-adsorbed H and attributed the high ΔG_{ad}^0 and low θ^0 to the lateral repulsion with underpotentially deposited H in hollow/bridge sites.³⁵ In alkaline solutions, OH or H₂O may co-adsorb with underpotentially deposited H, which could reduce the extent of H–H lateral repulsion, resulting in a reduction of ΔG_{ad}^0 from that in acid. This speculation needs to be verified in the future using *in situ* spectroscopic methods to identify the adsorbates.

Lastly, we compared the free energy diagrams of the dominant Tafel pathway for the HOR–HER in acid, and in base (Figure 6a), and show a shift in the optimal H–BE going from acid to base for the specific activity expressed by the Pt area-normalized exchange currents (Figure 6b). As illustrated using the Pt catalyst as an example, the standard activation free energies ($\Delta G_{\text{+T}}^{*0}$ and $\Delta G_{\text{−V}}^{*0}$) increase, and the H adsorption energy (ΔG_{ad}^0) decreases upon going from acid to base. Both changes lead to higher reaction barriers for all the reaction steps and, thus, result in HOR–HER activities lowered by 2 orders of magnitude. The most profound change is the activation barrier for the Volmer reaction, doubling from 177 to 352 meV (Figure 6a), suggesting that it is easier to adsorb and desorb H from and to hydrated protons in an acid than from and to H₂O molecules in a base. A DFT study found that the main contribution to the activation barrier for the Volmer reaction on the Pt(111) surface in acid comes from an initial proton transport from one water molecule to another before a proton can be transferred to the electrode,³⁹ i.e., consistent with an earlier model in which the Volmer reaction rate is governed by the reorientation of the water molecule that accepts the proton from the hydronium ion, H₃O⁺.⁴⁰ The superfast rate of proton transport is rationalized by the low intrinsic barrier along the hydrogen bond network.⁴¹ Thus, it is understandable that the lack of such a mechanism for OH[−] transport in alkaline solutions may cause an increase in the activation barrier for the Volmer reaction. In addition, the HO–H bond breaking/formation for water dissociation/recombination in base likely has a considerable activation barrier, differing from the virtually activation-less hydrogen bond breaking/formation for hydrated proton (H₂O–H⁺) in acid. Either one or both of these two catalyst-insensitive factors may account for the 2 order of magnitude difference in acid and base activities.

In comparing different catalysts, we note that with the increase being larger for $\Delta G_{\text{−V}}^{*0}$ than for $\Delta G_{\text{+T}}^{*0}$, the rate-determining step switches from the Tafel reaction in acid to the Volmer reaction in base. The impact on the HOR–HER specific activities for the Pt(bulk), Ru₁@Pt₁(2 ML), and Ru₁@Pt_{0.5}(1 ML) nanocatalysts is illustrated by the volcano plot in Figure 6b. While the Ru₁@Pt₁(2 ML) catalyst remains the most active in both acid and base (circles), the Pt(bulk) loses its also-top position in acid to become the least active in base (squares), and the Ru₁@Pt_{0.5}(1 ML) moves up from third to second place in going from acid to base (triangles). The lines drawn through the data points show a shift of the optimal H–BE to the weakening side from acid to base.

5. CONCLUSIONS

The HOR–HER activities we presented above largely are consistent with those determined using hydrogen fuel cells or

RDEs for Pt^{15,17} and for RuPt alloys.^{19,42} The advantages of the hanging-strip GDE method used here include the following. (1) It is a feasible way to alleviate the gas transport limitation in electrochemical kinetic measurements, thereby allowing the determination of the HOR–HER activities in acid, and providing a sufficient potential range for quantitative kinetic analyses. (2) It offers a more relevant performance test for membrane fuel cells and electrolyzers because the same GDE configuration (catalyst loadings, ink formula, and gas diffusion materials) can be used for studying the influence of GDE configuration on reaction kinetics.

For practical applications in AEM fuel cells and water electrolyzers, we demonstrated a factor of 4 enhancement in Pt mass activity using single-crystalline Ru₁@Pt₁(2 ML) core–shell nanoparticles compared to Pt nanoparticles. On the basis of total metal loading, the enhancement factor is 2.6. This increase doubles that on the Ru_{0.6}Pt_{0.4} alloy nanocatalysts, verifying the benefit of placing all the Pt atoms in the top two atomic layers. From temperature-dependent activities, we determined the apparent activation barriers. The ΔE_{a} values are 355 meV or 34.3 kJ mol^{−1} for Pt catalyst and 315 meV or 30.4 kJ mol^{−1} for the Ru₁@Pt₁(2 ML) catalyst, i.e., close to the activation free energies for the Volmer reaction, $\Delta G_{\text{−V}}^{*0}$, which is the rate-determining step in the dominant pathway.

New insights into the reaction mechanism and factors determining the HOR–HER activity were obtained by our kinetic analyses of the polarization curves using the dual-pathway kinetic model. For all three nanocatalysts, viz., Pt(bulk), Ru₁@Pt₁(2 ML), and Ru₁@Pt_{0.5}(1 ML), the Tafel reaction pathway (Tafel–Volmer for the HOR and Volmer–Tafel for the HER) dominates within ± 200 mV overpotentials. The 2 order of magnitude decrease in the HOR–HER activities going from acid to base is ascribed to one or both of the two catalyst-insensitive factors, the slower transport of OH[−] than of H⁺ in water, and the stronger O–H bond in water molecules (HO–H) than in hydrated protons (H₂O–H⁺). With a switch of the rate-determining step from the Tafel to the Volmer reaction going from acid to base, there is a shift to a weaker optimal hydrogen binding energy, making Ru₁@Pt₁(2 ML) a significantly better-than-Pt nanocatalyst for the HOR–HER in an alkaline environment.

AUTHOR INFORMATION

Corresponding Author

*E-mail: jia@bnl.gov.

Present Addresses

[†]K.E.: Department of Chemistry, University of Pennsylvania, 231 S. 34 St., Philadelphia, PA 19104.

[‡]J.H.: Institute of Plasma Physics, Chinese Academy of Sciences, P.O. Box 1126, Hefei 230031, P. R. China.

[§]G.C.: Institute of Advanced Chemical Power Sources, School of Chemical Engineering and Technology, Harbin Institute of Technology, 92 W. Da-Zhi St., Harbin 150001, China.

^{||}W.A.: College of Chemistry and Chemical Engineering, Shanghai University of Engineering Science, 333 Longteng Rd., Songjiang District, Shanghai 201620, China.

Notes

The authors declare no competing financial interest.

ACKNOWLEDGMENTS

This research was supported by the U.S. Department of Energy, Division of Chemical Sciences, Geosciences and Biosciences

Division, under Contract DE-SC0012704. The DFT calculations were performed using computational resources at the Center for Functional Nanomaterials, a user facility at Brookhaven National Laboratory. K.E. acknowledges the financial support from the U.S. Department of Energy, Office of Science, and Office of Workforce Development for Teachers and Scientists (WDTS) under the Science Undergraduate Laboratory Internships Program (SULI). J.H. acknowledges financial support from the Youth Innovation Promotion Association of the Chinese Academy of Sciences (2015265). Z.M. acknowledges financial support from the Natural Science Foundation of China (21336003) and the Major Basic Research Program of China (2014CB239703). G.C. acknowledges financial support from the China Scholarship Council.

ABBREVIATIONS

AEM, anion exchange membrane; CTR, charge transfer resistance; H-BE, hydrogen binding energy; OH-BE, hydroxide binding energy; DFT, density functional theory; GDE, gas diffusion electrode; GDL, gas diffusion layer; HER, hydrogen evolution reaction; HOR, hydrogen oxidation reaction; ML, monolayer; PEM, proton exchange membrane; PGM, platinum group metal; RDE, rotating disk electrode

REFERENCES

- (1) Gasteiger, H. A.; Kocha, S. S.; Sompalli, B.; Wagner, F. T. *Appl. Catal., B* **2005**, *56*, 9–35.
- (2) Debe, M. K. *Nature* **2012**, *486*, 43–51.
- (3) Lu, S.; Pan, J.; Huang, A.; Zhuang, L.; Lu, J. *Proc. Natl. Acad. Sci. U. S. A.* **2008**, *105*, 20611–20614.
- (4) Leng, Y.; Chen, G.; Mendoza, A. J.; Tighe, T. B.; Hickner, M. A.; Wang, C. Y. *J. Am. Chem. Soc.* **2012**, *134*, 9054–9057.
- (5) Slanac, D. A.; Lie, A.; Paulson, J. A.; Stevenson, K. J.; Johnston, K. P. *J. Phys. Chem. C* **2012**, *116*, 11032–11039.
- (6) Chung, H. T.; Won, J. H.; Zelenay, P. *Nat. Commun.* **2013**, *4*, 1922.
- (7) Holewinski, A.; Idrobo, J.-C.; Linic, S. *Nat. Chem.* **2014**, *6*, 828–834.
- (8) Sanetuntikul, J.; Shanmugam, S. *Nanoscale* **2015**, *7*, 7644–7650.
- (9) Yang, G.; Choi, W.; Pu, X.; Yu, C. *Energy Environ. Sci.* **2015**, *8*, 1799–1807.
- (10) Suntivich, J.; May, K. J.; Gasteiger, H. A.; Goodenough, J. B.; Shao-Horn, Y. *Science* **2011**, *334*, 1383–1385.
- (11) McCrory, C. C. L.; Jung, S.; Peters, J. C.; Jaramillo, T. F. *J. Am. Chem. Soc.* **2013**, *135*, 16977–16987.
- (12) Grimaud, A.; May, K. J.; Carlton, C. E.; Lee, Y.-L.; Risch, M.; Hong, W. T.; Zhou, J.; Shao-Horn, Y. *Nat. Commun.* **2013**, *4*, 2439.
- (13) Pandiarajan, T.; John Berchmans, L.; Ravichandran, S. *RSC Adv.* **2015**, *5*, 34100–34108.
- (14) Parrondo, J.; George, M.; Capuano, C.; Ayers, K. E.; Ramani, V. *J. Mater. Chem. A* **2015**, *3*, 10819–10828.
- (15) Sheng, W.; Gasteiger, H. A.; Shao-Horn, Y. *J. Electrochem. Soc.* **2010**, *157*, B1529–B1536.
- (16) Strmcnik, D.; Uchimura, M.; Wang, C.; Subbaraman, R.; Danilovic, N.; van der Vliet, D.; Paulikas, A. P.; Stamenkovic, V. R.; Markovic, N. M. *Nat. Chem.* **2013**, *5*, 300–306.
- (17) Durst, J.; Siebel, A.; Simon, C.; Hasché, F.; Herranz, J.; Gasteiger, H. A. *Energy Environ. Sci.* **2014**, *7*, 2255.
- (18) Alia, S. M.; Pivovar, B. S.; Yan, Y. *J. Am. Chem. Soc.* **2013**, *135*, 13473–13478.
- (19) Wang, Y.; Wang, G.; Li, G.; Huang, B.; Pan, J.; Liu, Q.; Han, J.; Xiao, L.; Lu, J.; Zhuang, L. *Energy Environ. Sci.* **2015**, *8*, 177–181.
- (20) Hsieh, Y.-C.; Zhang, Y.; Su, D.; Volkov, V.; Si, R.; Wu, L.; Zhu, Y.; An, W.; Liu, P.; He, P.; Ye, S.; Adzic, R. R.; Wang, J. X. *Nat. Commun.* **2013**, *4*, 2466.
- (21) Sheng, W.; Zhuang, Z.; Gao, M.; Zheng, J.; Chen, J. G.; Yan, Y. *Nat. Commun.* **2015**, *6*, 5848.
- (22) Gomez, R.; Orts, J. M.; Feliu, J. M. *J. Phys. Chem. B* **2004**, *108*, 228–238.
- (23) Garcia-Araez, N. *J. Phys. Chem. C* **2011**, *115*, 501–510.
- (24) Wang, J. X.; Zhang, Y.; Capuano, C. B.; Ayers, K. E. *Sci. Rep.* **2015**, *5*, 12220.
- (25) Kresse, G.; Hafner, J. *Phys. Rev. B: Condens. Matter Mater. Phys.* **1993**, *47*, 558–561.
- (26) Kresse, G.; Furthmüller, J. *Phys. Rev. B: Condens. Matter Mater. Phys.* **1996**, *54*, 11169–11186.
- (27) Blöchl, P. E. *Phys. Rev. B: Condens. Matter Mater. Phys.* **1994**, *50*, 17953–17979.
- (28) Kresse, G.; Joubert, D. *Phys. Rev. B: Condens. Matter Mater. Phys.* **1999**, *59*, 1758–1775.
- (29) Perdew, J. P.; Chevary, J. A.; Vosko, S. H.; Jackson, K. A.; Pederson, M. R.; Singh, D. J.; Fiolhais, C. *Phys. Rev. B: Condens. Matter Mater. Phys.* **1992**, *46*, 6671–6687.
- (30) Perdew, J. P.; Chevary, J. A.; Vosko, S. H.; Jackson, K. A.; Pederson, M. R.; Singh, D. J.; Fiolhais, C. *Phys. Rev. B: Condens. Matter Mater. Phys.* **1993**, *48*, 4978–4978.
- (31) Pack, J. D.; Monkhorst, H. J. *Phys. Rev. B* **1977**, *16*, 1748–1749.
- (32) Methfessel, M.; Paxton, A. T. *Phys. Rev. B: Condens. Matter Mater. Phys.* **1989**, *40*, 3616–3621.
- (33) Schlappa, A.; Lischka, M.; Gross, A.; Käsberger, U.; Jakob, P. *Phys. Rev. Lett.* **2003**, *91*, 016101.
- (34) Liu, P.; Logadottir, A.; Nørskov, J. K. *Electrochim. Acta* **2003**, *48*, 3731–3742.
- (35) Wang, J. X.; Springer, T. E.; Liu, P.; Shao, M.; Adzic, R. R. *J. Phys. Chem. C* **2007**, *111*, 12425–12433.
- (36) Wang, J. X.; Springer, T. E.; Adzic, R. R. *J. Electrochem. Soc.* **2006**, *153*, A1732–A1740.
- (37) Chen, S.; Kucernak, A. *J. Phys. Chem. B* **2004**, *108*, 13984–13994.
- (38) Wang, J. X.; He, P.; Zhang, Y.; Ye, S. *ECS Trans.* **2014**, *64*, 121–127.
- (39) Skúlason, E.; Karlberg, G. S.; Rossmeisl, J.; Bligaard, T.; Greeley, J.; Jónsson, H.; Nørskov, J. K. *Phys. Chem. Chem. Phys.* **2007**, *9*, 3241–3250.
- (40) Pecina, O.; Schmickler, W. *Chem. Phys.* **1998**, *228*, 265–277.
- (41) Guthrie, J. P. *J. Am. Chem. Soc.* **1996**, *118*, 12886–12890.
- (42) St. John, S.; Atkinson, R. W.; Unocic, R. R.; Zawodzinski, T. A., Jr.; Papandrew, A. B. *J. Phys. Chem. C* **2015**, *119*, 13481–13487.